Next Materials 4 (2024) 100195

Contents lists available at ScienceDirect

Next Materials

journal homepage: www.sciencedirect.com/journal/next-materials

Research article

Constructing oxygen-deficient shell on Li-rich cathodes by spark plasma sintering for high-performance lithium-ion batteries

Rui Wang [a,b,1], Zhongyuan Huang [a,1], Jia Zhang [a,1], Wenhai Ji [c,e], Xiaoyu Gao [a], Tao Zeng [a], Ziwei Chen [a], Maolin Yang [a], Wenguang Zhao [a], Tingting Yang [a,d,*], Lei Jin [d], Rafal E. Dunin-Borkowski [d], Juping Xu [c,e], Wen Yin [c,e], Fusheng Liu [f], Jun Wang [g], Yinguo Xiao [a,**]

[a] School of Advanced Materials, Peking University, Shenzhen Graduate School, Shenzhen 518055, China
[b] Department of Engineering, University of Cambridge, 17 Charles Babbage Road, Cambridge CB30FS, UK
[c] Institute of High Energy Physics, Chinese Academy of Sciences (CAS), Beijing 100049, China
[d] Ernst Ruska-Centre for Microscopy and Spectroscopy with Electrons, Forschungszentrum Jülich GmbH, Jülich 52428, Germany
[e] Spallation Neutron Source Science Center (SNSSC), Dongguan 523803, China
[f] College of Materials Science and Engineering, Shenzhen University, Shenzhen 518060, China
[g] School of Innovation and Entrepreneurship, Southern University of Science and Technology, Shenzhen 518055, China

ARTICLE INFO

Keywords:
Lithium-rich layered oxides
Lithium-ion batteries
Surface modification
Oxygen vacancies
Cycling stability

ABSTRACT

Lithium-rich layered oxides (LROs) are considered as promising cathodes in building next-generation lithium-ion batteries (LIBs) with superior charge-discharge capacity. Nevertheless, LROs are confronted with irreversible oxygen loss accompanied with surface-to-bulk degradation upon cycling. To inhibit the oxygen release and to increase the lifespan of LROs, we report on an innovative strategy to rapidly construct an ultrathin oxygen-deficient shell layer covering the surface of LROs' particles via a sparking plasma sintering (SPS) technique. It is demonstrated that the inner structure of the LROs' particles is maintained, whereas the surface of the particles forms a thin shell (~5 nm) consisting of a considerable amount of oxygen vacancies. Benefitting from the existence of an oxygen-deficient shell, the cathode activation is facilitated and the oxygen loss is suppressed, leading to enhanced capacity and prominent cyclability under long cycling. The modified LRO exhibits outstanding electrochemical performance, delivering a maximum capacity of 187.67 mAh g^{-1} and a capacity retention of 95.71% after 200 cycles at 250 mA g^{-1}. Our work evidences that SPS is a fast and effective approach to construct oxygen-deficient shell on LRO cathodes for high-performance LIBs.

1. Introduction

The research and development of energy storage devices, especially for application in electric vehicles (EVs), are in the ascendant with the vast developing foreground [1]. Consequently, rechargeable lithium-ion batteries (LIBs) have become the dominant power source to meet the ever-increasing market demands, triggering the development of various cathode materials [2–5]. Lithium-rich layered oxides (LROs) are considered as the most promising candidates for the next-generation LIBs, delivering a reversible capacity of ~250 mAh g^{-1} and a high energy density above 900 Wh kg^{-1} [6–9]. The high capacity of LROs is widely recognized to originate from anion redox reactions at high voltage together with inevitable O^{2-}/O^{-} migration in the lattice, resulting in undesirable structural evolution. [10–13] During lithiation or delithiation processes, interfacial reactions between cathode and electrolyte occur, resulting in the deterioration of materials. [14,15] The gradually accumulated irreversible structural degradation during cycling would aggravate capacity fade and voltage decay, thus eventually restricting the performance of LROs.

To address the issues of LROs mentioned above, tremendous efforts have been applied via the surface engineering method [16,17]. Traditional methods including surface doping and coating can stabilize the

---

[*] Corresponding author at: School of Advanced Materials, Peking University, Shenzhen Graduate School, Shenzhen 518055, China.
[**] Corresponding author.
E-mail addresses: t.yang@fz-juelich.de (T. Yang), y.xiao@pku.edu.cn (Y. Xiao).
[1] These authors contributed equally to this work.

https://doi.org/10.1016/j.nxmate.2024.100195
Received 11 January 2024; Received in revised form 1 April 2024; Accepted 2 April 2024

bulk or surface structure to some extent but with limited efficaciousness and in the sacrifice of reaction kinetics [18–21]. Based on these concerns, recent research on LROs has turned a spotlight on defect engineering strategy. Under this consideration, construction of oxygen vacancies (OVs) is one of the effective strategies [22]. By pre-introducing certain OVs to the surface of as-prepared LROs, oxygen loss and structure degradation can be suppressed dramatically during charging and discharging [23–25]. A major challenge of this strategy lies in the difficulty of controlling the oxygen deficiency shell constrained homogeneously on the surface of LROs without breaking the structural integrity of the interior. Most efforts implemented to crack this hard nut were made by chemical methods including annealing in reducing atmosphere and/or acid treatment [26–29]. Unfortunately, chemical procedures tend to be complicated, time-consuming and relatively expensive. As a consequence, it makes great sense to explore a more effective method for the quick construction of a surface oxygen-deficient layer.

In this work, we propose an innovative strategy based on spark plasma sintering (SPS) to artificially regulate an ultrathin oxygen-deficient shell on the as-synthesized Li-rich Mn-based layered oxides with remarkable effectiveness, as depicted in Fig. 1a. SPS is a fast and pressure-assisted sintering technique involving plasma activation and hot pressing. During SPS, a pulse current is also applied to powder particles from a special pulse generator. Benefiting from high-speed ion migration, the particle surface is purified by eliminating adsorptive impurities and gas. In a word, SPS has superiorities in much shorter sintering time, rapid heating and cooling rate, controllable conditions, and environmental friendliness, etc [30,31]. As a result, an oxygen-deficient layer with a thickness of about 5 nm is successfully constructed on the particle surface without compromising the structural integrity of the interior bulk, which is directly confirmed by combining structure and morphology characterizations. Furthermore, the electrochemical properties of the regulated LRO exhibit obvious improvements compared to the pristine sample, particularly for the extraordinary cycling stability. *Ex-situ* measurements during charge and discharge processes and after cycling are also carried out to analyze the effects of surface defects on structural and electrochemical behaviors. This simple and effective strategy to regulate the surface of Li-rich cathode material could bring some inspiration for fabricating long-life high-energy-density lithium-ion batteries.

2. Results and discussion

As illustrated in Fig. 1a, an oxygen-deficient shell is constructed on Li-rich cathode by the post-treatment with the SPS technique. The successful introduction of oxygen vacancies to the surface of LROs is unambiguously evidenced by a series of characterizations afterward. By taking advantage of the sensitivity of neutron powder diffraction (NPD) method, overall structural information such as atomic occupancies and defect concentration can be determined accurately owing to the superiority of neutron diffraction in distinguishing not only light elements like Li and O but also adjacent transition metal elements including Ni, Mn, and Co. As shown in Fig. 1b and Figure S1, the refined NPD patterns demonstrate that all peaks in each sample can be indexed with a rhombohedral $R\overline{3}m$ and a monoclinic $C2/m$ structure model, which fits well with the refined X-ray diffraction (XRD) patterns (Figure S2). The OVs percentages in the surface reconstructed LRO (S-LRO) are

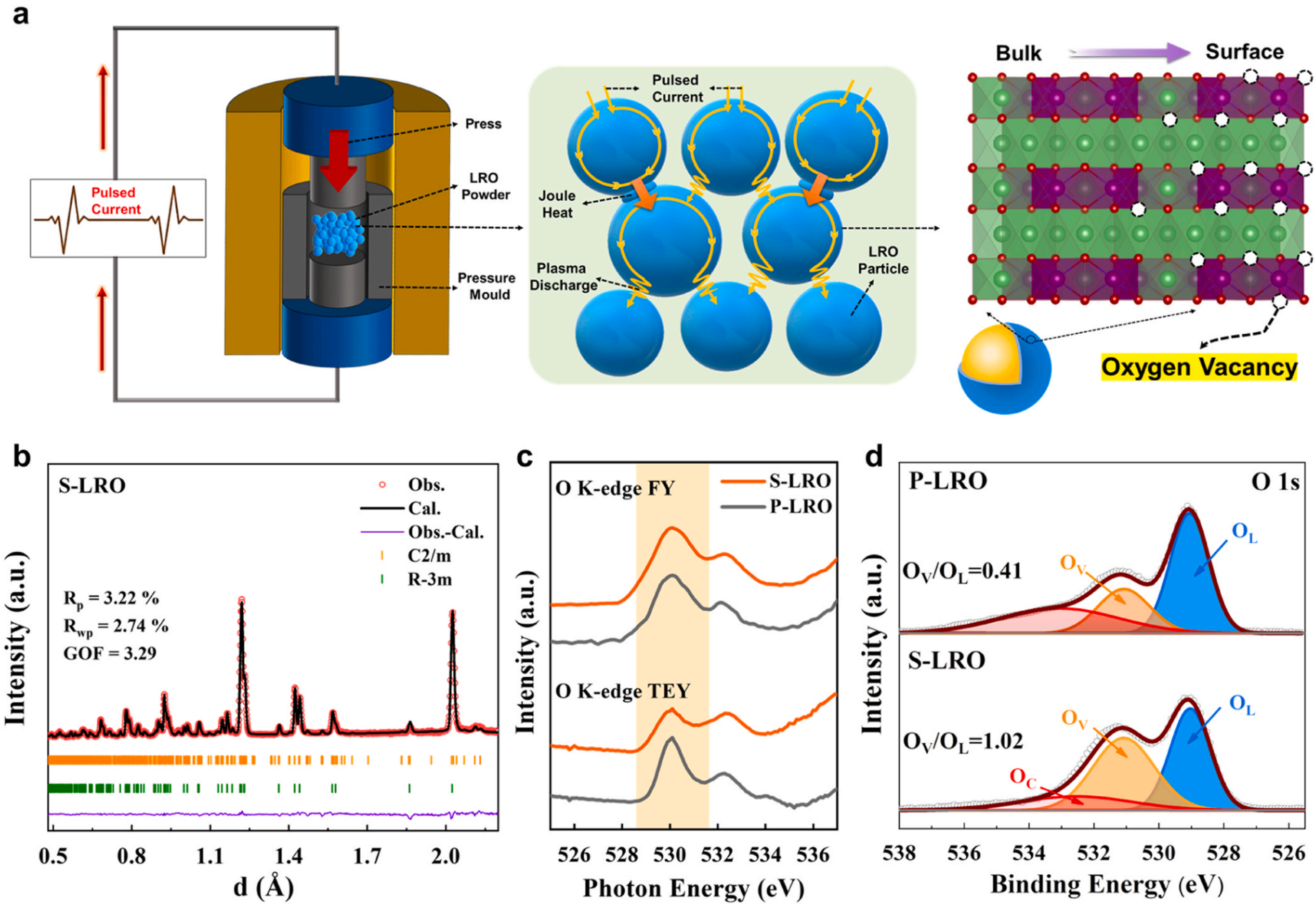

Fig. 1. (a) Schematic illustration of introducing OVs to the surface of S-LRO. (b) Observed and calculated NPD patterns for S-LRO. (c) XAS spectra of O K-edge for P-LRO and S-LRO at FY and TEY modes. (d) XPS spectra of the O 1 s for S-LRO and P-LRO.

determined to be 1.86(9)% on the 8*j* site and 2.10(6)% on the 4*i* site in the monoclinic $C2/m$ structure, while the pristine sample (P-LRO) exhibits 1.01(9)% on the 8*j* site and 1.26(6)% on the 4*i* site based on the Rietveld refinement results, evidencing that certain amount of lattice oxygen is lost during pulse current processing. Noticeably, lattice parameters and phase fractions do not differ significantly between S-LRO and P-LRO, owing to the fact that SPS treatment adjusts mostly the surface structure. For example, the contents of the hexagonal phase are 47.73(7)% in P-LRO and 47.00(7)% in S-LRO, which are close. The lattice parameters of S-LRO are $a = 2.8460(1)$ Å, $c = 14.2118(12)$ Å, which are slightly smaller than those of P-LRO with $a = 2.8476(1)$ Å, $c = 14.2207(12)$ Å. The c/a ratios of both samples are approximately 4.99, representing that a typical layered structure is well-maintained after SPS treatment. More details on the refined results from NPD are summarized in Table S1.

Based on the results discussed above, OVs are proven to be successfully introduced into S-LRO cathode through SPS process. Next, it is necessary to figure out the spatial distribution of OVs. As shown in Fig. 1c, the soft X-ray absorption spectroscopy (sXAS) data were collected in both TEY (total-fluorescence-yield) mode with the detection depth of several nanometers and FY (fluorescence-yield) mode with more than 100 nm depth [32] for the chemical states of elements on the surface and in the interior bulk of the particle, respectively. It turns out that P-LRO and S-LRO show almost the same O K-edge spectra at FY mode, indicating that the valence state of oxygen inside the particle remains unaltered. In contrast, at TEY mode, the O K-edge spectrum of S-LRO shows a lower peak intensity at about 530 eV in comparison with that of P-LRO, which is expected to be the result of OVs created on the surface by SPS. XPS spectra of the O 1 s peak without etching further substantiate this phenomenon, as depicted in Fig. 1d. The peaks at bonding energies of 529.05 eV, 531.28 eV, and 532.37 eV reveal the presence of lattice oxygen (O_L), oxygen vacancies (O_V), and chemisorbed oxygen (O_C) [33,34]. Notably, the O_V/O_L ratio for S-LRO is 1.02, significantly surpassing the 0.41 ratio observed for the P-LRO sample. This discrepancy implies a higher concentration of oxygen vacancies on the particle surface of the S-LRO sample in comparison to the P-LRO sample. This result is also consistent with the sXAS and confirms that more OVs are introduced into the particle surface to S-LRO through SPS treatment.

For further structural and chemical investigations, scanning electron microscopy (SEM) images were collected, and the results show similar morphology and elemental distributions between S-LRO and P-LRO

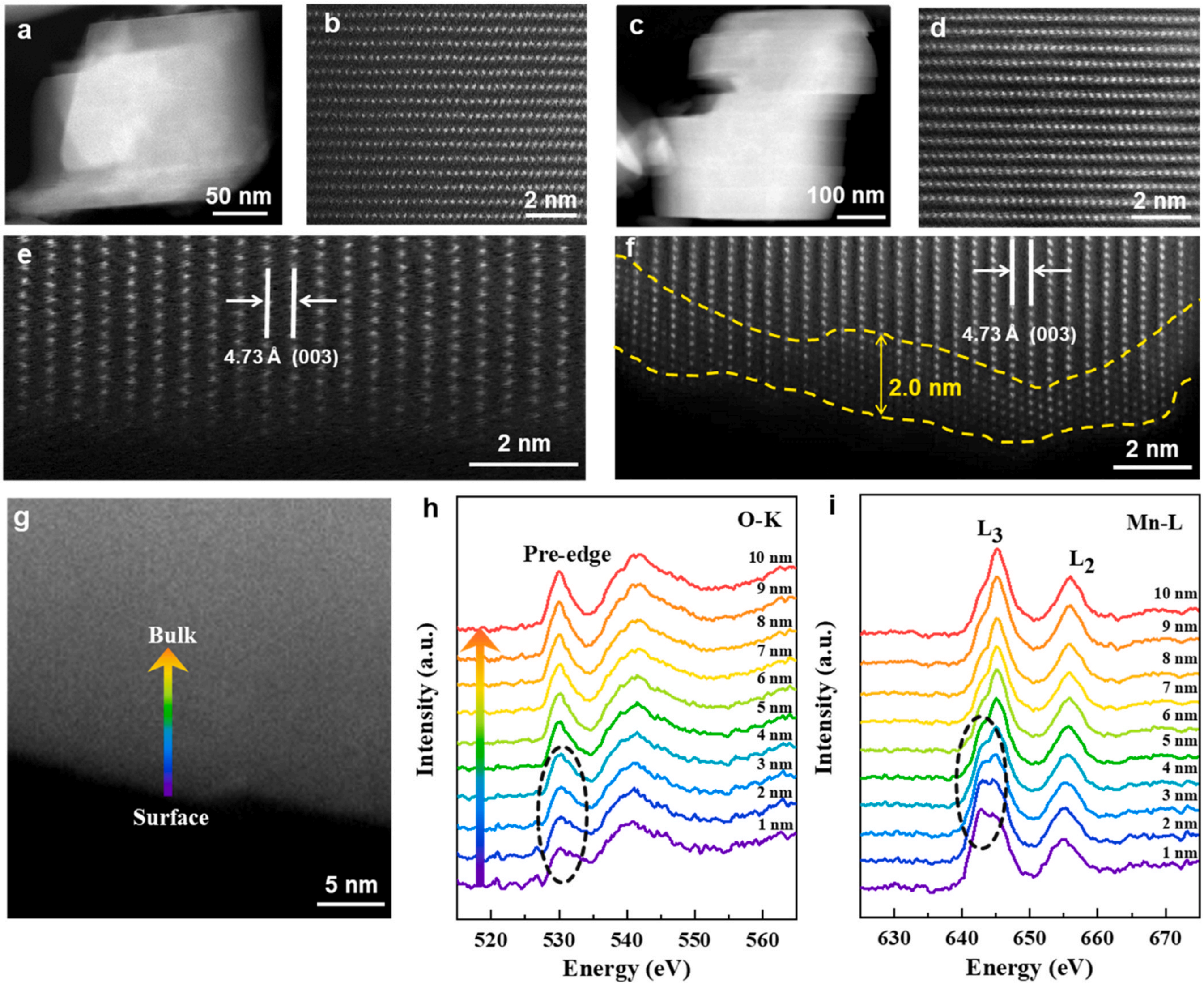

Fig. 2. HAADF-STEM images of (a) P-LRO and (c) S-LRO at low magnifications. Atom-resolved HAADF images in the bulk interior and on the particle surface for (b, e) P-LRO and (d, f) S-LRO. (g-i) EELS of O-K and Mn-$L_{2,3}$ edges of S-LRO as a function of positions along the arrow, starting from the surface to the interior. The interval for adjacent spectra is 1 nm.

particles (Figure S3 and S4). High-angle annular dark-field (HAADF) scanning transmission electron microscopy (STEM) images were chosen to visualize the altered surface structure at atomic resolution with EELS measurement for compositional change in the shell layer of particles. The results are shown in Fig. 2. Atom-resolved HAADF images in the bulk interior (Fig. 2b) and at the surface (Fig. 2e) were collected from the P-LRO particle (Fig. 2a). Apparently, P-LRO presents a uniformly layered structure without noticeable differences between the interior and surface. S-LRO shows an identical bulk structure with P-LRO (Fig. 2d), whereas, the surface structure appears differently, as can be seen in Fig. 2f, S5, and S6. Transition metal atoms occupy certain sites in Li layers, leading to the formation of a reconstructed layer with a thickness of about 2 nm. In addition, the (003) *d*-spacing is unchanged after SPS, which is consistent with the *c* values deduced from NPD. All these results imply that the SPS-induced cation mixing defects are only distributed in the thin layer around the surface. Electron energy loss spectroscopy (EELS) measurements are also performed to compare the compositional difference with the increase of distance from the particle surface. Fig. 2g illustrates the selected area of S-LRO particle for EELS measurements, and the pre-edge peak at ∼530 eV can be ascribed to the electron transition from O 1 s core state to the unoccupied 2p states in Fig. 2h [35]. From the surface to the bulk, the O K-edge spectra show a gradual strengthening in relative intensity of the pre-edge peak (Fig. 2h and S7), suggesting that oxygen vacancies are mainly accumulated on the surface owing to the alteration of oxygen local environment [36,37]. Fig. 2i presents the EELS spectra of Mn $L_{2,3}$ edges, showing a reduced Mn valence state on the surface. Specifically, L_3/L_2 ratios, as displayed in Figure S8, show that the valence of Mn remains lower at approximately 5 nm distance away from the surface, which is expected to compensate for the charge imbalance caused by OVs [38]. To further study the Mn valence state before and after SPS-treatment, XPS measurements are conducted for two P-LRO and S-LRO cathode which is shown in Figure S9. From the fitting results for the XPS spectrum for two samples, we find that the valence state of all the Mn is +4, which is consistent with the theoretical valence state of Mn in Li-rich cathode. However, there is 7.3% Mn^{3+} in the S-LRO cathode with the SPS-treatment which is also consistent with the EELS results. Furthermore, the surface state can be further analyzed by the ratio between the integrating peaks area of O and Mn spectra (denote O/Mn ratio). In Figure S8b, the O/Mn ratio shows a clear increase from the surface to the interior, verifying that the regulation of the oxygen-deficient layer is about 5 nm. In contrast, the EELS spectra of the O/Mn ratio for P-LRO sample keep almost

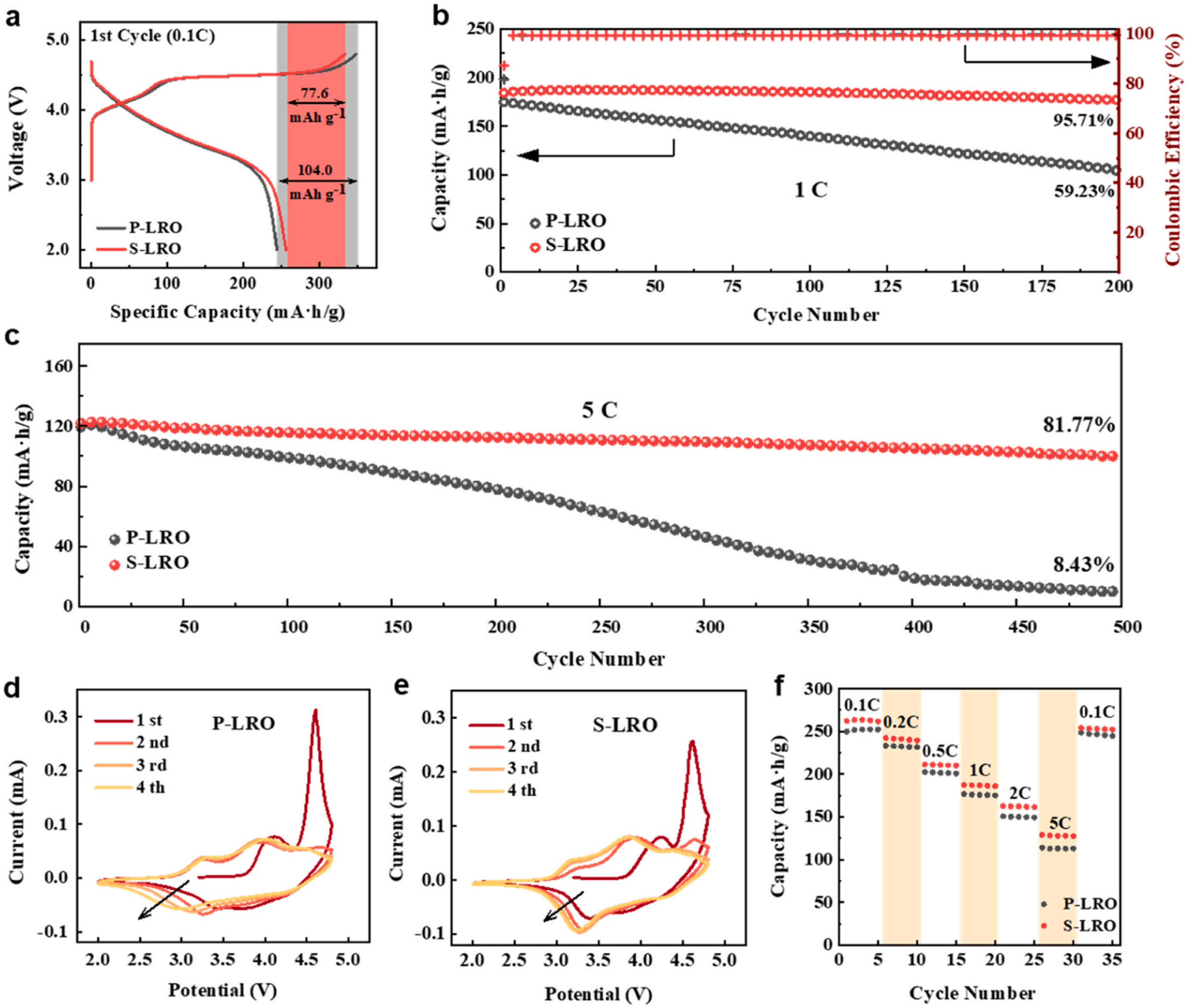

Fig. 3. (a) Initial charge/discharge curves of P-LRO and S-LRO at 0.1 C (1 C = 250 mA g^{-1}) from 2.0 to 4.8 V. Cycling performance of P-LRO and S-LRO at (b) 1 C over 200 cycles and (c) 5 C over 500 cycles. Cyclic voltammetry curves of (d) P-LRO and (e) S-LRO. (f) Rate capabilities of P-LRO and S-LRO.

unchanged from the particle surface to the inner region as shown in Figure S10. Meanwhile, high-resolution in-depth XPS tests are also conducted for P-LRO cathode and S-LRO cathode which is shown in Figure S11. The XPS spectra is normalized by the OVs peak (Figure S11a-b) and peak intensity ratio for OVs peak/ TM-O peak are also calculated at different etching depth for two sample shown in Figure S11c. The variation pattern of peak intensity ratio with depth further confirmed that the oxygen-deficient layer is about 5 nm for S-LRO cathode. Accordingly, STEM, EELS and previous NPD analyses jointly confirm the successful control of oxygen-deficient layer, which is expected to have a positive influence on structural stability and enhance electrochemical performance. Through SPS, a simple and time-saving technique is successfully realized without the influence on particle integrity.

In order to explore the influence of surface reconstruction on electrochemical performance, half cells with lithium metal as anode and P-LRO or S-LRO as cathode were assembled and investigated. Fig. 3a displays the initial charge-discharge curves of the cells using P-LRO and S-LRO as cathodes at 25 mA g^{-1}. The typical long plateau at about 4.5 V stands for the activation of lattice oxygen in LROs, contributing to the major of charge capacity [39]. To be gratified, both the discharge capacity and initial Coulombic efficiency of S-LRO exhibit a higher level compared to those of P-LRO. The discharge specific capacities of P-LRO and S-LRO are 244.4 mAh g^{-1} and 256.0 mAh g^{-1}, respectively. Irreversible capacity loss of S-LRO (77.6 mAh g^{-1}) is much less than that of P-LRO (104.0 mAh g^{-1}) as highlighted in Fig. 3a, suggesting fewer surface side reactions with electrolyte and less oxygen loss thanks to the presence of OVs on the particle surface. Long-term cycling performance is evaluated to explore the structure stability corresponding to surface deficiencies. Interestingly, the specific discharge capacity of S-LRO shows a slight increase to 187.67 mAh g^{-1} in the first 25 cycles at 1 C (see Fig. 3b). It is remarkable that S-LRO displays a capacity of 177.2 mAh g^{-1} even after 200 cycles at 1 C, in stark contrast to the remained capacity of merely 104.3 mAh g^{-1} for P-LRO. Obviously, the S-LRO cathode with SPS treatment harvests outstanding capacity retention of 95.71% after 200 cycles at 1 C.

The extraordinary cycling stability is comparable to the best electrochemical performance of Li-rich cathode $Li_{1.2}Mn_{0.54}Ni_{0.13}Co_{0.13}O_2$ reported in literature as listed in Table S2. In addition, S-LRO sample can slow down the voltage decay to a certain degree and ultimately achieve a higher energy density (Figure S12). Moreover, as shown in Fig. 3c, P-LRO cathode exhibits a dramatic capacity fading after 500 cycles at a high rate of 5 C, whereas S-LRO cathode still retains a superior capacity of 81.77%, which should benefit from the surface reconstruction alleviating the capacity fading. The existence of surface OVs assists in pre-activating Li_2MnO_3 phase and thus reducing the energy barrier of Li ions diffusion and irreversible capacity loss in the initial cycle. [40] The partial pressure of oxygen on the surface can be reduced by the pre-activated surface layer of S-LRO sample with OVs. Consequently, gaseous oxygen is prevented from evolving during plateau charging. In addition, OVs reduce the amounts of active oxygen on the surface and suppress the lattice oxygen loss, leading to less abominable surface reactions between electrolyte and particle at the interface dramatically and more capacity compensation.

The corresponding cyclic voltammetry (CV) curves of P-LRO and S-LRO for the initial four cycles are plotted in Fig. 3d and e, respectively. An obviously smaller electrochemical polarization can be observed in S-LRO, accompanied by different oxygen anions oxidation peaks and Mn cations redox peaks. The modified LRO is conductive to inhibiting Mn-ions dissolution and stabilizing the structure according to better overlapping of Mn^{4+}/Mn^{3+} redox peaks. On the other hand, the oxidation peak of oxygen anions for S-LRO at ~4.6 V is weaker than P-LRO during the initial cycle, standing for retarded oxygen loss, less cathode-electrolyte interfacial reactions and optimized structure reversibility in S-LRO cathode. Moreover, the existence of more OVs can provide higher possibilities for Li^+ to escape from the tetrahedral sites, facilitating the kinetics of Li^+ inserting/extracting at the surface of particle. Consequently, S-LRO delivers a better rate capability than P-LRO from 0.1 C to 5 C (see Fig. 3f). According to calculated results from EIS measurements (Figure S13), the Li^+ diffusion coefficient (D_{Li+}) of S-LRO (2.2×10^{-13} $cm^2\cdot s^{-1}$) is higher than that of P-LRO (0.6×10^{-13} $cm^2\cdot s^{-1}$) before cycling and the charge transfer resistance of S-LRO is still smaller than P-LRO after 200 cycles. Meanwhile, the galvanostatic intermittent titration technique (GITT) tests of the first discharge process for S-LRO and P-LRO cathode are conducted which is shown in Figure S14. The GITT calculation results also clearly indicate the Li^+ diffusion coefficient of S-LRO is higher than that of P-LRO cathode. Based on all the above results it can be concluded that the surface reconstruction of the ultrathin oxygen-deficient shell plays an essential role in promoting the Li^+ diffusion kinetics at the cathode-electrolyte interface.

To figure out the underlying mechanism associated with improved electrochemical behaviors, *ex-situ* XAS spectroscopy was conducted to track the electronic states of oxygen at a series of charging/discharging voltages during the first cycle. The pre-edge peak of oxygen between 525 eV and 535 eV stands for the transition from O 1 s to Mn_{3d}-O_{2p} hybridized states. [41–43] It consists of two peaks representing the excitation from O_{2p} to unoccupied $t_{2\,g}$ orbitals at ~530 eV and e_g orbitals at ~531 eV. The broad peak above 535 eV corresponds to the hybridization of Mn_{4sp}-O_{2p} [44]. As demonstrated in Fig. 4a, by comparing with the XAS spectra before cycling, a great decrease is observed in the sXAS O K-edge spectra (TEY) of P-LRO cathode at the pre-edge peak ~530 eV upon charging to high voltages from 4.2 V to 4.8 V. The result manifests that the chemical states of oxygen on the particle surface change significantly with the occurrence of some interfacial reactions for P-LRO. Another specific reason responsible for this phenomenon is that surface reactions lower the valence of Mn and thus boost the excitation of electrons in $t_{2\,g}$ orbitals and weaken the hybridization strength of Mn_{3d}-O_{2p} [45,46]. Moreover, a peak at ~534 eV is also observed at the 2.0 V discharged state for P-LRO, which can be indexed to the carbonate group ($-CO_3$). The formation of compounds such as Li_2CO_3 on the particle surface impedes the sustainability of subsequent cycles with respect to the decomposition of electrolyte and serious surface side reactions.

In comparison to the initial state, the O K-edge spectra of S-LRO under TEY mode after charging to the voltage plateau at 4.5 V exhibits a different profile. It tends to be reversible upon further charging to 4.8 V, as shown in Fig. 4b. The optimized structure reversibility benefits from the pre-construction of ultrathin O-deficient shell before cycling, which has been confirmed by the contrast between O K-edge of S-LRO before charging at TEY and FY modes previously (Fig. 1c). Fig. 4c displays the integrated intensity around 532 eV of oxidized oxygen at TEY mode, which is normalized by the first peak at ~530 eV as shown in Figure S15. The results further prove that OVs on the surface stabilize the oxygen valences at different electrochemical states according to the minor fluctuation of integrated intensity for S-LRO. The sXAS of O K-edge at different charging/discharging states were also performed at FY mode for both P-LRO and S-LRO samples, as shown in Fig. 4d and e. The whole series of spectra do not show prominent change during the initial cycling for both P-LRO and S-LRO cathodes, suggesting that the oxidation states and local environment of oxygen ions in the bulk keep basically unchanged. The conclusion can be verified by Fig. 4f, where the normalized integrated intensity around 532 eV is compared at FY mode. Both electrodes show similar tendencies throughout the charge and discharge processes except for minor irregular fluctuations. Based on the analysis above, the ultrathin O-deficient layer on the surface can be deduced to play a crucial role in mitigating interfacial reactions during cycling.

From the viewpoint of crystal structure evolution, the corresponding *in-situ* XRD patterns at 0.2 C during the first cycling were investigated to gain more insights into the protective effect of ultrathin O-deficient layers. As shown in Fig. 5, P-LRO and S-LRO electrodes exhibit a similar evolution trend on the offset of peak positions. A relatively large shift of

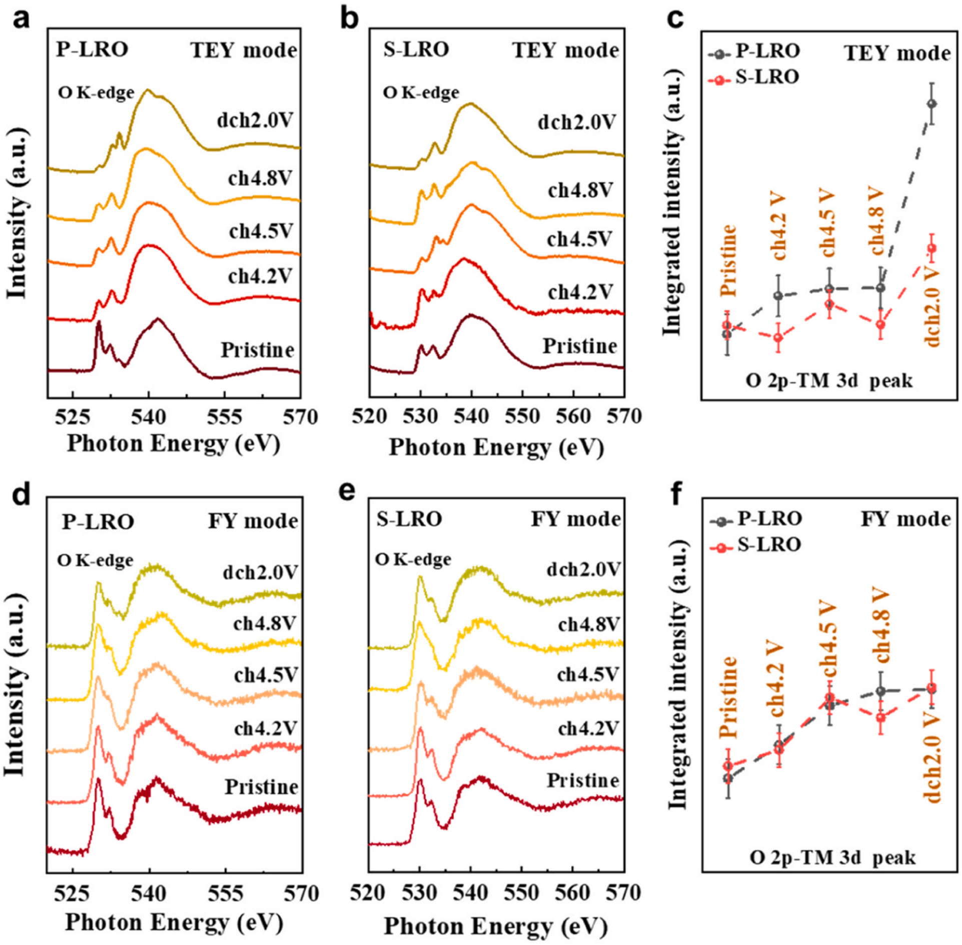

Fig. 4. XAS spectra of O K-edge for (a, d) P-LRO and (b, e) S-LRO at (a, b) TEY and FY (d, e) modes during the first cycle at 0.1 C. (c, f) Peak area evolutions of oxygen oxidation for (c) P-LRO and (f) S-LRO during the first cycle. All the peak areas are normalized with the peak area of P-LRO in the pristine state under TEY and FY modes.

(003) reflection to the lower scattering angle after charging to 4.8 V can be seen from Fig. 5a for P-LRO, which indicates the extensive expansion of *c*-axis due to the increased electrostatic repulsion between adjacent O layers during the Li^+ extraction, and the irreversible structure transition with the production of disordered structures. [47–50] The intercalation path is altered during the first cycling, as the study reports previously, Li ions are hindered to get back to the transition metal layer with respect to the structural alteration. [48] The evolution of lattice parameter *c* in both samples is extracted from *in-situ* XRD patterns and exhibited in Fig. 5b and d. It was monitored that the lattice parameter *c* expands 0.87% at the full charge state and a totally of 0.32% along *c* axis after first cycling for S-LRO. In comparison, P-LRO manifests a corresponding increase of 0.93% in lattice parameter *c* at a full state-of-charge and a totally of 0.37% along *c* axis after discharging. To sum up, S-LRO exhibits a satisfying structural reversibility after discharging to 2.0 V for the similar position of (003) reflection with the pristine state. It can be speculated that the OVs maintain the relatively consistent O-O electrostatic repulsion and reduce the decomposition of Li_2MnO_3 domains. [51, 52] Once the structure evolution is alleviated, the sustainable long cycle life could be maintained.

In situ differential electrochemical mass spectrometry (DEMS) was employed to elucidate the positive impacts of SPS treatment on gas evolution and interfacial protection. As depicted in Fig. 6a and b, the DEMS results reveal a distinct O_2 release for the P-LRO sample, particularly evident during high-voltage charging. In contrast, the S-LRO sample exhibits significantly lower O_2 release, even under high voltage, a finding consistent with the O-K Edge sXAS results. Concurrently, the CO_2 evolution during the initial charge and discharge cycle indicates reduced CO_2 release for the S-LRO sample compared to the P-LRO sample. This reduction could be attributed to the mitigation of irreversible oxygen release and the suppression of side reactions at the cathode-electrolyte interface. These findings collectively validate that the oxygen-deficient shells induced by SPS treatment in the LRO cathode effectively suppress gas release and parasitic reactions on the particle surface. To elucidate the better electrochemical reversibility of the modified cathode particle from the perspective of structure failure, the cycled electrodes were analyzed. Fig. 6c shows the XPS spectra of Mn 2p for P-LRO sample before cycling and after 200 cycles at 1 C. It is evident that all Mn ions have a typical valence state of +4 with Mn $2p_{3/2}$ at 642.7 eV and Mn $2p_{1/2}$ at 654.2 eV, which matches with other reports [53]. However, the binding energies of the two peaks shift to 641.9 and 653.5 eV after cycling, implying the occurrence of a serious phase transition from layered structure to spinel-like or rock-salt type structure, accompanied with the generation of a considerable amount of Mn^{3+}. On the contrary, S-LRO displays a small amount of Mn^{3+} before cycling with Mn $2p_{3/2}$ and Mn $2p_{1/2}$ at 642.3 and 653.8 eV (Fig. 6d), which is in accordance with the spinel-like phase observed in TEM (Figure S6b) and EELS (Fig. 2i) results. The ultrathin spinel-like shell on the surface acts as a protection layer to accommodate lattice strain. Comparatively, the difference of the binding energies of Mn 2p before and after cycling for S-LRO is far smaller than that of P-LRO, revealing a retarded phase transition on the cathode particle surface. In addition, XPS spectra of Li anodes extracted from the coin cells cycled for 200 cycles at 1 C were measured to prove that the modified S-LRO sample

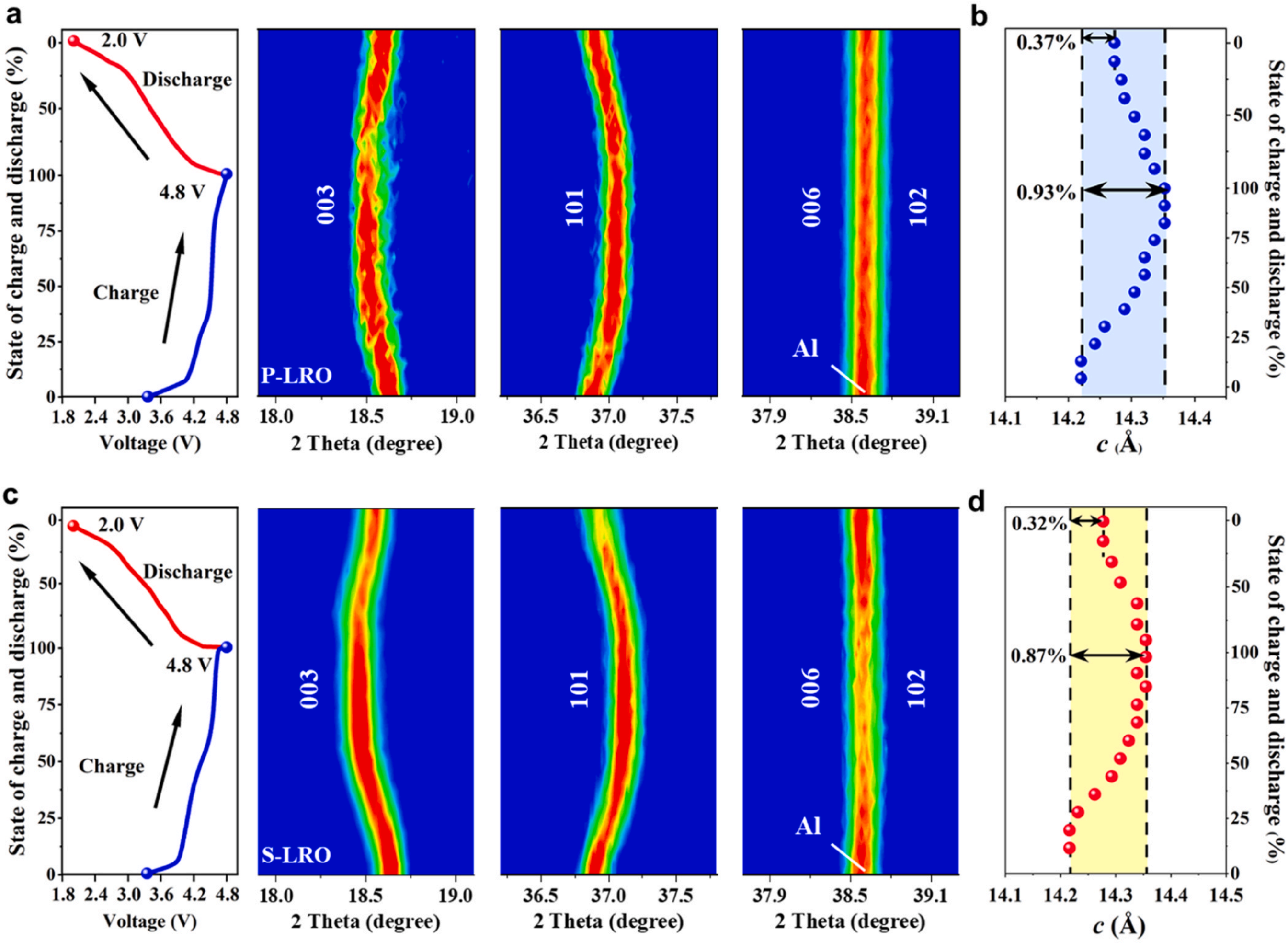

Fig. 5. *In-situ* XRD patterns of (a) P-LRO and (c) S-LRO during the first cycle at 0.2 C with the corresponding charge-discharge curves on the left. The evolutions of lattice parameter *c* fitted by *in-situ* XRD patterns for (b) P-LRO and (d) S-LRO.

can reduce Mn ions dissolution effectively upon cycling, as indicated in Figure S16. The Li anode cycled for 200 cycles retains its metallic luster for S-LRO and no Mn signal can be detected on the particle surface, compared with obvious Mn signal for P-LRO. In addition, the electrolyte of LRO coin cell after long-term cycling is also diluted and used for the ICP-OES tests. From the ICP-OES measurement results (Figure S17) we can know that there are much more Mn ions dissolution in the electrolyte for P-LRO cathode compared to the S-LRO cathode. It can be inferred that the dissolution of Mn ions is one of the main reasons responsible for the LRO cathode degradation process, which can be prevented effectively by introducing surface OVs.

Structure evolutions of both samples were analyzed by *ex-situ* XRD patterns at different cycle numbers at 1 C to understand the role of O-deficient layers in stabilizing the lattice structure, as indicated in Figure S18 and S19. The (003) peak position of S-LRO remains almost unchanged after 200 cycles compared with that of P-LRO. The lattice parameter *c* expands from 14.236 Å to 14.340 Å for P-LRO with an increment of 0.73% after cycling, whereas, S-LRO manifests a corresponding increase of only 0.23%. TEM and SEM images (Figure S20) acquired after 200 cycles deliver more straightforward information for the structure stability after SPS treatment. As exhibited in Fig. 6e, P-LRO particle has a mass of cracks with local lattice distortion and an amorphous phase on the surface. The cracks inevitably accelerate the surface side reaction with electrolyte and collapse of the whole structure. Conversely, the particle of S-LRO sample is almost unbroken with an intact layered structure in the bulk (Fig. 6f), matching the *ex-situ* XPS spectra. It also gives solid proof for enhanced long-cycling stability in the electrochemical analysis part for S-LRO.

To further investigate whether the SPS method can effectively control the concentration and thickness of the O vacancy, the effect of temperature as the key parameter in the SPS experiment on the thickness of the O vacancy for LRO cathode is systematically studied. A series of EELS and electrochemical tests are also conducted for the LRO cathode with different sintering temperature during SPS process. (Figure S21 and Figure S22) And from the EELS results for the LRO cathode with different sintering temperature during SPS process, we find that by increasing the SPS treatment temperature, the thickness of oxygen vacancies is effectively increased which indicate that the SPS method can easily control the thickness of the O vacancy for LRO cathode. And combined with the electrochemical test results for the LRO cathode with different sintering temperature during SPS process, we conclude that moderate amount of oxygen vacancies in LRO cathode particle surface can serve as an effective protective layer to inhibit oxygen release and facilitate the kinetics of Li^+ inserting/extracting at the surface which will significantly improve the cyclic stability of LRO cathode.

3. Conclusions

In summary, oxygen-deficient shells are constructed at the surface of Li-rich cathode particles by adopting a novel and efficient SPS post-treatment strategy. The side reactions with electrolyte are partially suppressed in SPS-treated Li-rich cathodes during the initial cycle owing

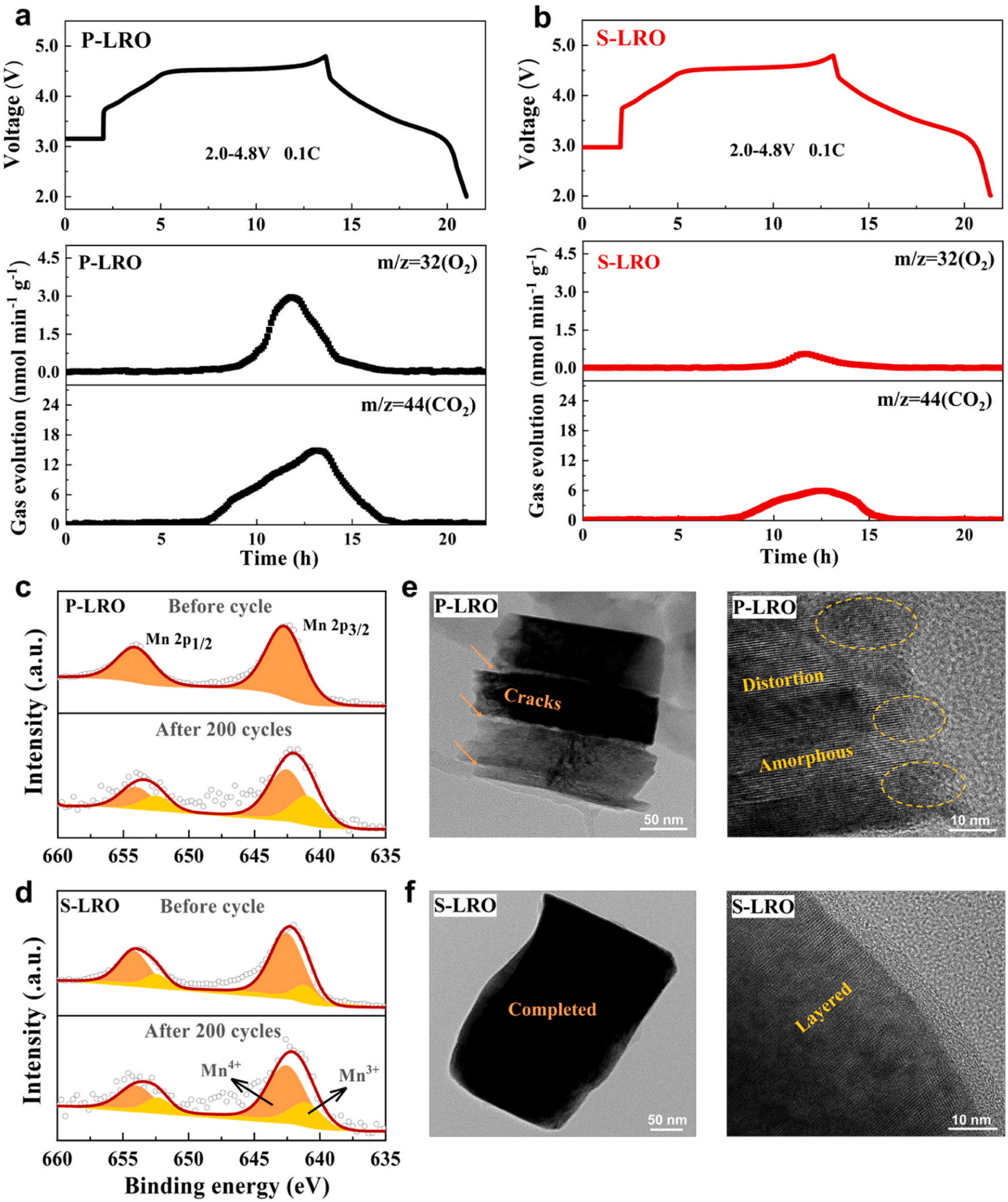

Fig. 6. *In situ* DEMS results of (a) P-LRO and (b) S-LRO. *Ex-situ* Mn 2p XPS spectra of (c) P-LRO and (d) S-LRO before and after 200 cycles. TEM images of (e) P-LRO and (f) S-LRO after 200 cycles at 1 C acquired at different magnifications.

to the successful establishment of the ultrathin oxygen-deficient layers in the particle surface without affecting the bulk structure. This oxygen-deficient shell with a thickness about 5 nm contributes to fast Li^+ diffusion kinetics at the interface by promoting more Li^+ to escape from the tetrahedral site traps, resulting in a better rate capability and higher discharge capacity. More importantly, oxygen-deficient layers accompanied with cation disorders enhance the long-term cycle and voltage stability effectively by suppressing oxygen loss and structural deterioration in the Li-rich layered materials. The surface modification also reduces the stress accumulation during long cycling, leading to enhanced cyclability with less degradation in LRO cathode. To the best of our knowledge, this work put forward a simple, efficient, and mass-produced SPS technique for pre-introducing controllable oxygen vacancies to enhance the electrochemical performance of Li-rich cathodes. We believe this universal methodology can shed some light on surface modification of cathode materials towards the research and development of safer and more stable LIBs.

4. Experimental section

The precursor $Mn_{2/3}Co_{1/6}Ni_{1/6}CO_3$ was prepared by the co-precipitation method. First, a solution of $MnSO_4·4\ H_2O$, $NiSO_4·6\ H_2O$ and $CoSO_4·7\ H_2O$ with a concentration of 2.0 mol L^{-1} were stirred well in the reactor. Then, a 2.0 mol L^{-1} Na_2CO_3 and NH_4OH solution were added. The stirring temperature was held at 60 ℃ with a fixed pH value of 7.8. The sediments were washed with water several times and dried at 80 °C in a vacuum oven to get a powder precursor. After that, the precursor was well ground with Li_2CO_3 (5% excess) by ball-milling thoroughly at low rotation speed of 100 rpm for 4 hours to make sure the precursors can keep the secondary spheres morphology. Subsequently, the resulting mixture was transferred to a furnace for preheating at 480 ℃ for 5 h and then calcinated at 850 ℃ for 12 h in the air. The chemical formula of the as-prepared pristine sample (P-LRO) is $Li_{1.2}Mn_{0.54}Ni_{0.13}Co_{0.13}O_2$. The SPS-treated sample (S-LRO) was acquired by simply adding a post-treatment for P-LRO, which applied the SPS technology. For the SPS treatment process, the as-prepared pristine sample was packed into a graphite die with inner diameter of 10 mm, and the graphite paper was used as the inner lining for graphite die to prevent side reactions between samples and graphite die. Then the graphite dies with sample inside placed in the chamber of the SPS equipment which was evacuated down to a low air pressure about 10^{-3} Pa. After that, the sample was heated from 25 ℃ to 300 ℃ within 6 min (corresponding heating rate: 50 ℃·min^{-1}) with direct current pulses of 2 ms followed by 2 ms rest time (the output current is 1500 A and the output voltage is 10 V, corresponding to output power of 15 kW). Meanwhile, the pressurization device is set to 4.7 KN (corresponding pressure is 60 MPa). After the heated to 300 ℃, a dwell step at 300 ℃ for 30 min was realized and followed by a controlled cooling whining 6 min to room temperature. So, the total synthesis/sintering time is about 42 minutes. Then the block was move from the graphite die and then ground in a mortar to get a fine powder.

Sample morphologies were characterized by ZEISS Supra 55 scanning electron microscopy (SEM) and JEOL-3200FS field-emission transmission electron microscopy (FE-TEM) carried out at 300 kV, equipped with Energy Dispersive Spectroscopy (EDS) to obtain elements distribution. Atomic-scale microstructure characterization and electron energy loss spectroscopy (EELS) experiments were performed on a Cs corrected FEI Titan G2 ChemiSTEM 80–200 TEM with a field emission gun. The operating voltage was accelerated to 200 kV. The convergence semi-angle for HAADF STEM images was around 25 mrad and the collection semi-angle was 70–200 mrad. For the crystal structure investigations, both X-ray powder diffraction (XRD) and neutron powder diffraction (NPD) patterns were collected. XRD was carried out on a Bruker D8 ADVANCE diffractometer with a Cu Kα source ($\lambda = 1.5406$ Å) including pristine powder characterization and in-situ experiments. NPD was performed on the Multi-Physics Instrument (MPI) [54] at China Spallation Neutron Source (CSNS), Dongguan China. Each pattern was collected for 1.531 h to ensure the quality of data. Rietveld refinements of both XRD and NPD results were performed by the FullProf Suite program. [55] X-ray photoelectron spectroscopy (XPS, ESCA Lab220I-XL) measurement was conducted by a focused monochromatic with Al Kα X-ray source to analyze the valence states of Mn, Ni, and O. Undoubtedly, C 1 s peak at 284.8 eV were used to calibrate each spectrum. O K-edge soft X-ray absorption spectroscopy (sXAS) spectra were performed at the Russian-German Dipole Beamline (RGBL) at the BESSY II electron storage ring operated by the Helmholtz-Zentrum Berlin für Materialien und Energie [56]. Both fluorescence yield (FY) mode and total electron yield (TEY) mode were measured at $T = 300$ K at 10^{-9} Torr (UHV).

CR2032 button cells were used to measure electrochemical performance. The procedures of preparing cathode electrodes were detailed as follows: 80 wt% cathode material, 10 wt% acetylene black and 10 wt% PVDF were dissolved in N-methyl-2-pyrrolidone (NMP) solvent. Then, the well-stirred slurries were coated on aluminum foils uniformly, followed by drying in a vacuum oven at 120 ℃ for 12 h. The active material mass loading was controlled at around 5.0 mg·cm^{-2}. The assembly of the half-cell was carried out in a glove box filled with argon gas. The electrolyte was comprised of 1 M $LiPF_6$ in EC, EMC, and DMC with equal volume. Celgard 2325 membrane was chosen as the separator with lithium metal foil employed as the anode. Galvanostatic charge-discharge cycling was conducted in the voltage range of 2.0–4.8 V on the Neware battery cycler at different rates (1 C = 250 mA·g^{-1}). Cyclic voltammetry (CV) and electrochemical impedance spectroscopy (EIS) were performed on the electrochemical workstation (CHI660E). CV tests were conducted at 0.1 mV s^{-1} between 2.0 and 4.8 V and EIS was investigated with a voltage amplitude of 5 mV in the frequency range of $0.1-10^5$ Hz. The OEMS was performed using Swagelok-type cells assembled within a glovebox. In this experimental setup, Argon (BOC N6.0), pre-purified using a Bronkhorst purifier before flow control, served as the carrier gas. The gas line was linked to a quadrupole mass spectrometer (Pfeiffer) via a heated capillary (120 ℃) to prevent condensation. The charge and discharge processes were regulated by an electrochemical workstation (Ivium).

For ICP-OES analysis, LRO||Li-metal coin cells were constructed with 120 μL of electrolyte with glass fiber separators which can absorb more electrolyte. After both cells cycled for 200 times, LRO||Li-metal coin cells were disassembled in an Ar filled glovebox and the separators were extracted, placed in a 15 mL polypropylene tube and centrifuged at 5000 rpm for 10 min. After remove separators, the 4.0 mL of ~2% nitric acid (diluted from concentrated nitric acid; 67−69%, trace metal grade, Fischer Chemical) was added to the extracted electrolyte before analysis.

Declaration of Competing Interest

The authors declare that they have no known competing financial interests or personal relationships that could have appeared to influence the work reported in this paper.

Acknowledgements

The research was financially supported by the National Key R&D Program of China (2020YFA0406203), National Natural Science Foundation of China (No. 52072008), Guangdong Basic and Applied Basic Research Foundation (Grant No. 2022B1515120070 and 2022A151510816) and the Large Scientific Facility Open Subject of Songshan Lake, Dongguan, Guangdong (Grant No. KFKT2022A04). The Major Science and Technology Infrastructure Project of Material Genome Big-science Facilities Platform supported by Municipal Development and Reform Commission of Shenzhen. The authors appreciate the beamtime at MPI granted from China Spallation Neutron Source (CSNS). We appreciate Huaican Chen and Yuanguang Xia for technical assistance during the neutron diffraction experiments. We are also grateful for the allocation of beamtime at RGBL Dipole beamline, BESSY II, HZB, Germany. And we would like to thank Dr. Dmitry Smirnov for the kindly assistance with sXAS measurements at the RGBL beamline of BESSY-II.

Appendix A. Supporting information

Supplementary data associated with this article can be found in the online version at doi:10.1016/j.nxmate.2024.100195.

References

[1] Y.L. Ding, Z.P. Cano, A.P. Yu, J. Lu, Z.W. Chen, Automotive Li-ion batteries: current status and future perspectives, Electrochem. Energy Rev. *2* (1) (2019) 1–28.

[2] R.C. Massé, E. Uchaker, G.Z. Cao, Beyond Li-ion: electrode materials for sodium- and magnesium-ion batteries, Sci. China-Mater. *58* (9) (2015) 715–766.

[3] Y.H. Zhou, H.F. Cui, B. Qiu, Y.H. Xia, C. Yin, L.Y. Wan, Z.P. Shi, Z.P. Liu, Sufficient oxygen redox activation against voltage decay in Li-rich layered oxide cathode materials, ACS Mater. Lett. *3* (4) (2021) 433–441.

[4] Z.Y. Lun, B. Ouyang, D.H. Kwon, Y. Ha, E.E. Foley, T.Y. Huang, Z.J. Cai, H. Kim, M. Balasubramanian, Y.Z. Sun, et al., Cation-disordered rocksalt-type high-entropy cathodes for Li-ion batteries, Nat. Mater. *20* (2) (2021) 214–221.

[5] B. Zhu, W. Zhang, Q.Y. Wang, Y.Q. Lai, J.Q. Zheng, N.F. Wen, Z. Zhang, Understanding the air-exposure degradation chemistry of the sacrificial cathode additive Li5FeO4for Li-ion batteries, Adv. Funct. Mater. (2024) 2315010.

[6] M.M. Thackeray, S.H. Kang, C.S. Johnson, J.T. Vaughey, R. Benedek, S.A. Hackney, Li2MnO3-stabilized LiMO2 (M = Mn, Ni, Co) electrodes for lithium-ion batteries, J. Mater. Chem. *17* (30) (2007) 3112–3125.

[7] H. Zhao, W.Y.A. Lam, L. Sheng, L. Wang, P. Bai, Y. Yang, D.S. Ren, H. Xu, X.M. He, Cobalt-free cathode materials: families and their prospects, Adv. Energy Mater. *12* (16) (2022) 2103894.

[8] J. Wang, X. He, E. Paillard, N. Laszczynski, J. Li, S. Passerini, Lithium- and manganese-rich oxide cathode materials for high-energy lithium ion batteries, Adv. Energy Mater. *6* (21) (2016) 1600906.

[9] S.H. Li, C.H. Guan, W. Zhang, H.X. Li, X.G. Gao, S. Zhang, S.M. Li, Y.Q. Lai, Z. Zhang, Stabilized anionic redox by rational structural design from surface to bulk for long-life fast-charging Li-rich oxide cathodes, Small 19 (2023) 2303539.

[10] E.M. Erickson, H. Sclar, F. Schipper, J. Liu, R.Y. Tian, C. Ghanty, L. Burstein, N. Leifer, J. Grinblat, M. Talianker, et al., High-temperature treatment of li-rich cathode materials with ammonia: improved capacity and mean voltage stability during cycling, Adv. Energy Mater. *7* (2017) 1700708.

[11] Z. Zhu, R. Gao, I. Waluyo, Y.H. Dong, A. Hunt, J. Lee, J. Li, Stabilized Co-free Li-rich oxide cathode particles with an artificial surface preconstruction. Adv. Energy Mater. *10* (2020) 2001120.

[12] J. Xu, M.L. Sun, R.M. Qiao, S.E. Renfrew, L. Ma, T.P. Wu, S. Hwang, D. Nordlund, D. Su, K. Amine, et al., Elucidating anionic oxygen activity in lithium-rich layered oxides, Nat. Commun. *9* (2018) 947.

[13] Q. Chen, Y. Pei, H.W. Chen, Y. Song, L. Zhen, C.Y. Xu, P.H. Xiao, G. Henkelman, Highly reversible oxygen redox in layered compounds enabled by surface polyanions, Nat. Commun. *11* (2020) 3411.

[14] S. Lee, W. Jin, S.H. Kim, S.H. Joo, G. Nam, P. Oh, Y.K. Kim, S.K. Kwak, J. Cho, Oxygen vacancy diffusion and condensation in lithium-ion battery cathode materials, Angew. Chem. -Int. Ed. *58* (31) (2019) 10478–10485.

[15] H.S. Liu, K.J. Harris, M. Jiang, Y. Wu, G.R. Goward, G.A. Botton, Unraveling the rapid performance decay of layered high-energy cathodes: from nanoscale degradation to drastic bulk evolution, Acs Nano *12* (3) (2018) 2708–2718.

[16] X.Q. Ji, Q. Xia, Y.X. Xu, H.L. Feng, P.F. Wang, Q.Q. Tan, A review on progress of lithium-rich manganese-based cathodes for lithium-ion batteries, J. Power Sources *487* (2021).

[17] P. Oh, J. Yun, S. Park, G. Nam, M.L. Liu, J. Cho, Recent advances and prospects of atomic substitution on layered positive materials for lithium-ion battery, Adv. Energy Mater. *11* (15) (2021) 2003197.

[18] H. Li, F.C. Meng, S.Y. Zhang, L.G. Wang, M. Li, L. Ma, W.N. Zhang, W.L. Zhang, Z. H. Yang, T.P. Wu, et al., Crystal-growth-dominated fabrication of metal-organic frameworks with orderly distributed hierarchical porosity, Angew. Chem. -Int. Ed. *59* (6) (2020) 2457–2464.

[19] L.G. Wang, X.C. Lei, T.C. Liu, A. Dai, D. Su, K. Amine, J. Lu, T.P. Wu, Regulation of surface defect chemistry toward stable Ni-rich cathodes, Adv. Mater. *34* (19) (2022) 2200744.

[20] M.J. Wang, F.D. Yu, G. Sun, J. Wang, J.G. Zhou, D.M. Gu, Z.B. Wang, Co-regulating the surface and bulk structure of Li-rich layered oxides by a phosphor doping strategy for high-energy Li-ion batteries, J. Mater. Chem. A *7* (14) (2019) 8302–8314.

[21] W. Zhang, Y.G. Sun, H.Q. Deng, J.M. Ma, Y. Zeng, Z.Q. Zhu, Z.S. Lv, H.R. Xia, X. Ge, S.K. Cao, et al., Dielectric polarization in inverse spinel-structured Mg2TiO4 coating to suppress oxygen evolution of li-rich cathode materials, Adv. Mater. *32* (19) (2020) 202000496.

[22] Y.H. Zhang, D. Zhang, L.R. Wu, J. Ma, Q. Yi, Z.X. Wang, X.F. Wang, Z. Wu, C. Zhang, N.F. Hu, et al., Stabilization of lattice oxygen in Li-rich Mn-based oxides via swing-like non-isothermal sintering, Adv. Energy Mater. *12* (43) (2022) 2202341.

[23] K. Chai, J.C. Zhang, Q.Y. Li, D. Wong, L.R. Zheng, C. Schulz, M. Bartkowiak, D. Smirnov, X.F. Liu, Facilitating reversible cation migration and suppressing O2 escape for high performance Li-rich oxide cathodes, Small *18* (18) (2022) 2201014.

[24] B. Qiu, M.H. Zhang, L.J. Wu, J. Wang, Y.G. Xia, D.N. Qian, H.D. Liu, S. Hy, Y. Chen, K. An, et al., Gas-solid interfacial modification of oxygen activity in layered oxide cathodes for lithium-ion batteries, Nat. Commun. *7* (2016) 12108.

[25] Z.K. Tang, Y.F. Xue, G. Teobaldi, L.M. Liu, The oxygen vacancy in Li-ion battery cathode materials, Nanoscale Horiz. *5* (11) (2020) 1453–1466.

[26] S.H. Kang, C.S. Johnson, J.T. Vaughey, K. Amine, M.M. Thackeray, The effects of acid treatment on the electrochemical properties of 0.5 Li2MnO3•0.5 LiNi0.44Co0.25Mn0.31O2 electrodes in lithium cells. J. Electrochem. Soc. *153* (6) (2006) A1186–A1192.

[27] K. Kubota, T. Kaneko, M. Hirayama, M. Yonemura, Y. Imanari, K. Nakane, R. Kanno, Direct synthesis of oxygen-deficient Li2MnO3 for high capacity lithium battery electrodes, J. Power Sources *216* (2012) 249–255.

[28] Z.C. Ye, B. Zhang, T. Chen, Z.G. Wu, D.Q. Wang, W. Xiang, Y. Sun, Y.X. Liu, Y. Liu, J. Zhang, et al., A simple gas-solid treatment for surface modification of li-rich oxides cathodes, Angew. Chem. -Int. Ed. *60* (43) (2021) 23248–23255.

[29] J.Q. Zhao, R.M. Huang, W.P. Gao, J.M. Zuo, X.F. Zhang, S.T. Misture, Y. Chen, J. V. Lockard, B.L. Zhang, S.M. Guo, et al., An ion-exchange promoted phase transition in a Li-excess layered cathode material for high-performance lithium-ion batteries, Adv. Energy Mater. *5* (9) (2015) 1401937.

[30] Z.Y. Hu, Z.H. Zhang, X.W. Cheng, F.C. Wang, Y.F. Zhang, S.L. Li, A review of multi-physical fields induced phenomena and effects in spark plasma sintering: fundamentals and applications, Mater. Des. (2020) *191*.

[31] T. Zhou, H. Wang, Y. Wang, P.X. Jiao, Z.M. Hao, K. Zhang, J. Xu, J.B. Liu, Y.S. He, Y.X. Zhang, et al., Stabilizing lattice oxygen in slightly Li-enriched nickel oxide cathodes toward high-energy batteries, Chem *8* (10) (2022) 2817–2830.

[32] R.M. Qiao, L.A. Wray, J.H. Kim, N.P.W. Pieczonka, S.J. Harris, W.L. Yang, Direct Experimental probe of the Ni(II)/Ni(III)/Ni(IV) redox evolution in LiNi0.5Mn1.5O4 electrodes, J. Phys. Chem. C. *119* (49) (2015) 27228–27233.

[33] K.Z. Gu, D.D. Wang, C. Xie, T.H. Wang, G. Huang, Y.B. Liu, Y.Q. Zou, L. Tao, S. Y. Wang, Defect-rich high-entropy oxide nanosheets for efficient 5-hydroxymethylfurfural electrooxidation, Angew. Chem. -Int. Ed. *60* (37) (2021) 20253–20258.

[34] Q. Wang, M. Yao, A.P. Zhu, H. Wu, Y. Zhang, Semi-metallic superionic layers suppressing voltage fading of Li-rich layered oxide towards superior-stable Li-ion batteries, Angew. Chem. -Int. Ed. *62* (37) (2023) e202309049.

[35] Y. Koyama, T. Mizoguchi, H. Ikeno, I. Tanaka, Electronic structure of lithium nickel oxides by electron energy loss spectroscopy, J. Phys. Chem. B *109* (21) (2005) 10749–10755.

[36] L.Z. Li, E. Self, D. Darbar, L.F. Zou, I. Bhattacharya, D.H. Wang, J. Nanda, C. M. Wang, Hidden subsurface reconstruction and its atomic origins in layered oxide cathodes, Nano Lett. *20* (4) (2020) 2756–2762.

[37] D.N. Qian, B. Xu, M.F. Chi, Y.S. Meng, Uncovering the roles of oxygen vacancies in cation migration in lithium excess layered oxides, Phys. Chem. Chem. Phys. *16* (28) (2014) 14665–14668.

[38] S.J. Zheng, R. Huang, Y. Makimura, Y. Ukyo, C.A.J. Fisher, T. Hirayama, Y. Ikuhara, Microstructural changes in LiNi0.8Co0.15Al0.05O2 positive electrode material during the first cycle, J. Electrochem. Soc. *158* (4) (2011) A357–A362.

[39] Y. Sun, H.J. Cong, L. Zang, Y.X. Zhang, Oxygen vacancies and stacking faults introduced by low-temperature reduction improve the electrochemical properties of Li2MnO3 nanobelts as lithium-ion battery cathodes, ACS Appl. Mater. Interfaces *9* (44) (2017) 38545–38555.

[40] Y.X. Cai, L. Ku, L.S. Wang, Y.T. Ma, H.F. Zheng, W.J. Xu, J.T. Han, B.H. Qu, Y. Z. Chen, Q.S. Xie, D.L. Peng, Engineering oxygen vacancies in hierarchically Li-rich layered oxide porous microspheres for high-rate lithium ion battery cathode, Sci. China-Mater. *62* (10) (2019) 1374–1384.

[41] J. Graetz, A. Hightower, C.C. Ahn, R. Yazami, P. Rez, B. Fultz, Electronic structure of chemically-delithiated LiCoO2 studied by electron energy-loss spectrometry, J. Phys. Chem. B *106* (6) (2002) 1286–1289.

[42] M. Oishi, K. Yamanaka, I. Watanabe, K. Shimoda, T. Matsunaga, H. Arai, Y. Ukyo, Y. Uchimoto, Z. Ogumi, T. Ohta, Direct observation of reversible oxygen anion redox reaction in Li-rich manganese oxide, Li2MnO3, studied by soft X-ray absorption spectroscopy, J. Mater. Chem. A *4* (23) (2016) 9293–9302.

[43] W.S. Yoon, M. Balasubramanian, K.Y. Chung, X.Q. Yang, J. McBreen, C.P. Grey, D. A. Fischer, Investigation of the charge compensation mechanism on the electrochemically Li-ion deintercalated Li1-xCo1/3Ni1/3Mn1/3O2 electrode system by combination of soft and hard x-ray absorption spectroscopy, J. Am. Chem. Soc. *127* (49) (2005) 17479–17487.

[44] J.G. Zhou, D. Hong, J. Wang, Y.F. Hu, X.H. Xie, H.T. Fang, Electronic structure variation of the surface and bulk of a LiNi0.5Mn1.5O4 cathode as a function of state of charge: X-ray absorption spectroscopic study, Phys. Chem. Chem. Phys. *16* (27) (2014) 13838–13842.

[45] E.Y. Hu, X.Q. Yu, R.Q. Lin, X.X. Bi, J. Lu, S.M. Bak, K.W. Nam, H.L.L. Xin, C. Jaye, D.A. Fischer, et al., Evolution of redox couples in Li- and Mn-rich cathode materials and mitigation of voltage fade by reducing oxygen release, Nat. Energy *3* (8) (2018) 690–698.

[46] T.G. Lin, T.U. Schulli, Y.X. Hu, X.B. Zhu, Q.F. Gu, B. Luo, B. Cowie, L.Z. Wang, Faster activation and slower capacity/voltage fading: a bifunctional urea treatment on lithium-rich cathode materials, Adv. Funct. Mater. *30* (13) (2020) 1909192.

[47] K. Nakayama, R. Ishikawa, S. Kobayashi, N. Shibata, Y. Ikuhara, Dislocation and oxygen-release driven delithiation in Li2MnO3, Nat. Commun. *11* (1) (2020) 4452.

[48] A. Singer, M. Zhang, S. Hy, D. Cela, C. Fang, T.A. Wynn, B. Qiu, Y. Xia, Z. Liu, A. Ulvestad, et al., Nucleation of dislocations and their dynamics in layered oxide cathode materials during battery charging, Nat. Energy *3* (8) (2018) 641–647.

[49] L.G. Wang, A.V. Dai, W.Q. Xu, S. Lee, W. Cha, R. Harder, T.C. Liu, Y. Ren, G.P. Yin, P.J. Zuo, et al., Structural distortion induced by manganese activation in a lithium-rich layered cathode, J. Am. Chem. Soc. *142* (35) (2020) 14966–14973.

[50] H.D. Liu, Y. Chen, S. Hy, K. An, S. Venkatachalam, D.N. Qian, M.H. Zhang, Y. S. Meng, Operando lithium dynamics in the li-rich layered oxide cathode material via neutron diffraction, Adv. Energy Mater. *6* (7) (2016) 201502143.

[51] H.Y. Li, N. Zhang, J. Li, J.R. Dahn, Updating the structure and electrochemistry of Li_xNiO_2 for $0 \leq x \leq 1$. J. Electrochem. Soc. *165* (13) (2018) A2985–A2993.

[52] T.C. Liu, J.J. Liu, L.X. Li, L. Yu, J.C. Diao, T. Zhou, S.N. Li, A. Dai, W.G. Zhao, S. Y. Xu, et al., Origin of structural degradation in Li-rich layered oxide cathode, Nature *606* (7913)) (2022) 305–312.

[53] S.T. Guo, S.X. Zhao, K. Bi, Y.F. Deng, K. Xiong, C.W. Nan, Research on electrochemical properties and fade mechanisms of Li-rich cathode materials at low-temperature, Electrochim. Acta *222* (2016) 1733–1740.

[54] B. Zhou, F. Shen, Z.L. Hu, S.L. Wang, X.C. Ruan, T.J. Liang, A study of stray neutron field measurements for the neutron scattering instruments at CSNS, Appl. Sci. -Basel *12* (10) (2022).

[55] J. Rodriguezcarvajal, Recent advances in magnetic-structure determination by neutron powder diffraction, Phys. B *192* (1-2) (1993) 55–69.

[56] S.L. Molodtsov, S.I. Fedoseenko, D.V. Vyalikh, I.E. Iossifov, R. Follath, S. A. Gorovikov, M.M. Brzhezinskaya, Y.S. Dedkov, R. Püttner, J.S. Schmidt, et al., High-resolution Russian-German beamline at BESSY, Appl. Phys. a-Mater. Sci. Process. *94* (3) (2009) 501–505.